Comparative Evaluation of Modulation Schemes for Grid-connected Parallel Interleaved Inverters

Ghanshyamsinh Gohil, Lorand Bede, Remus Teodorescu, Tamas Kerekes, Frede Blaabjerg
Department of Energy Technology, Aalborg University, Denmark
gvg@et.aau.dk

***Abstract*—A comparative evaluation of the different modulation schemes for the grid-connected converter with two parallel interleaved Voltage Source Converters (VSCs) is presented in this paper. The volume and the losses of the converter-side inductor of the LCL harmonic filter are evaluated for the grid-side converter of the multi-MW Wind Energy Conversion System (WECS). In order to achieve high current rating in MW-level WECS, two-level VSCs are often connected in parallel. The parallel connected VSCs can be operated with interleaved carrier signals and can be treated as a multi-level converter. As a result, the size of the harmonic filter components can be significantly reduced. However, circulating current flows between the parallel VSCs and it is often suppressed using a Coupled Inductor (CI). The losses and size of the CI are also evaluated for different modulation schemes and compared in this paper. A detailed discussion on the loss modeling of the inductive components and a multi-objective optimization method is also presented.**

***Index Terms*—Voltage source converters (VSC), filter design, multi-objective optimization, harmonic filter, pulse width modulation, interleaving, phase disposition modulation**

I. Introduction

The full scale power converter is often used in modern Wind Energy Conversion System (WECS) due to its ability to provide the reactive power compensation and a smooth grid connection for the entire speed range, and it is generally realized using three-phase two-level pulsewidth modulated Voltage Source Converter (VSC) [1]. The general trend is to use wind turbines with high output power (multi-megawatt scale) [2] and it is realized by connecting two-level VSCs in parallel. The switching frequency of the semiconductor devices employed in these high power systems is often limited. As a result, large filters are required in order to meet the stringent power quality requirements imposed by the utility [3]. When large filter components are used, considerable losses occur in the filter components and the overall conversion efficiency is compromised. They also result in increased cost of the overall converter system [4]. For a given switching frequency, the size of the harmonic filter components can be reduced by using multi-level converter.

For the parallel connected VSCs, multi-level voltage waveforms can be achieved by interleaving the carrier signals. The grid-side converter of the WECS with two parallel VSCs is shown in Fig. 1. The switched output voltage (hereafter referred as pole voltage and represent the potential difference between the ac output terminal of the VSC and the fictitious mid-point of the dc-link O) of each of the VSCs has two voltage levels ($+V_{\rm dc}/2$ and $-V_{\rm dc}/2$), as shown in Fig. 2(a). When the carrier signals are interleaved, the pole voltages of the corresponding phases of the individual VSCs are also phase shifted with respect to each other by an interleaving angle. For the parallel VSCs, the resultant switched output voltage is the average of the pole voltages of the individual VSCs and it exhibits three-level voltage waveforms, as shown in Fig. 2(b). This leads to reduction in the values of the harmonic filter components [5], [6]. However the circulating current flows between the parallel VSCs due to the control asymmetry, dead-time and the impedance mismatch [7], [8]. With the interleaved carrier signals, full dc-link voltage appears across the close path for a relatively longer duration (this duration could be as large as half of the switching period) [9], [10]. This will further aggravate the already existing problem of the

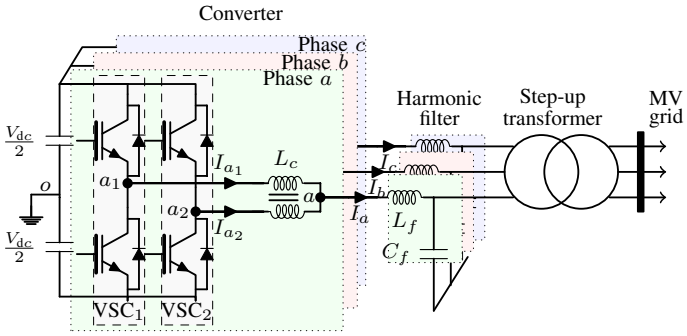

Fig. 1. Grid-side full-scale frequency converter for high power wind turbines using two parallel two-level voltage source converters.

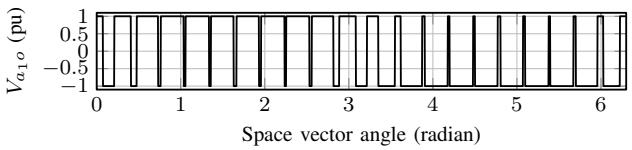

(a)

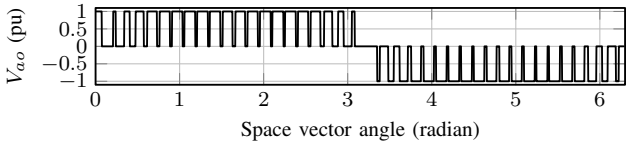

(b)

Fig. 2. Switched output voltage. (a) Pole voltage of one of the VSC, (b) Resultant output voltage of two parallel VSCs with interleaved carrier signals.

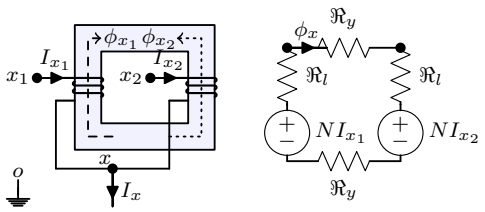

Fig. 3. Coupled inductor. Subscript x represents the phases a, b, and c. (a) Physical arrangement, (b) Simplified reluctance model.

circulating current and would lead to an increase in the losses and unnecessary over-sizing of the components present in the circulating current path. Therefore, the circulating current should be suppressed to some acceptable limit.

A Coupled Inductor (CI) can be used for this purpose [11], as shown in Fig. 1. Thanks to the magnetic coupling between the parallel interleaved legs of the corresponding phases, the CI offers high inductance to the circulating current and suppresses it effectively [12]. However, in addition to the LCL filter, another inductive component in terms of the CI is needed in such system. The size of the inductive components can be reduced by integrating the functionalities of the CI and the converter-side inductance of the LCL filter [13]–[17]. However, the discussion in this paper is limited to separate CI and converter-side inductor case, as shown in Fig. 1.

The harmonic performance of the resultant output voltage is significantly influenced by the Pulse-Width Modulation (PWM) scheme. Moreover, the losses and the size of the harmonic filter components and the CI are also significantly influenced by the PWM scheme. This paper evaluates the impact of different PWM schemes on the harmonic filter components and the CI. It is organized as follows: Section II briefly discusses the operation of the parallel VSCs and the different PWM schemes considered in this paper. The harmonic performance of the PWM schemes and the volume of the harmonic filter components are evaluated and compared in Section III. The losses and the volume of the CI for different PWM schemes are compared in Section IV.

II. Modulation of the Parallel Interleaved VSCs

The operation and the modulation of the parallel interleaved VSCs are presented in this section.

A. Operation of Parallel Interleaved VSCs

The grid-side converter with two parallel VSCs is shown in Fig. 1. The carrier signals of the parallel VSCs are interleaved by 180° and the CI is used for the circulating current suppression, as shown in Fig. 1. The physical arrangement of the CI is shown in Fig. 3. The core is made up of two limbs, which are magnetically coupled to each other by using the top and the bottom yokes. Both the limbs carry coils with the N number of turns and the coils are wound in the same direction. The starting terminals of both the coils are connected to the output of the respective VSC legs x_1 and x_2 and other terminals of both of the coils are connected together to form common connection point x, as shown in Fig. 1 and Fig. 3(a). The voltage across the coils of the CI are given as

$$\begin{aligned} V_{x_1x} &= R_{CI}I_{x_1} + L_s\frac{dI_{x_1}}{dt} - L_m\frac{dI_{x_2}}{dt} \\ V_{x_2x} &= R_{CI}I_{x_2} + L_s\frac{dI_{x_2}}{dt} - L_m\frac{dI_{x_1}}{dt} \end{aligned} \tag{1}$$

where R_{CI} is the resistance of the CI coil, L_s is the self inductance, L_m is the mutual inductance. The mutual inductance $L_m = kL_s$, where $0 \leq k \leq 1$. For the parallel VSCs, the leg current can be decomposed into two components:

1) Common current component ($I_x/2$, assuming equal current sharing).
2) Circulating current component $I_{x,c}$.

Therefore, the leg currents can be represented as

$$I_{x_1} = \frac{I_x}{2} + I_{x,c} \text{ and } I_{x_2} = \frac{I_x}{2} - I_{x,c} \tag{2}$$

Using (1), the difference of the pole voltages of the corresponding phase is given as (refer Fig. 1)

$$V_{x_1o} - V_{x_2o} = R_{CI}(I_{x_1} - I_{x_2}) + (L_s + L_m)\frac{d}{dt}(I_{x_1} - I_{x_2}) \tag{3}$$

obtaining $I_{x,c}$ from (2) and substituting in (3) yields

$$V_{x_1o} - V_{x_2o} = 2R_{CI}I_{x,c} + 2(L_s + L_m)\frac{dI_{x,c}}{dt} \tag{4}$$

similarly, taking the average of the pole voltages of the respective phases of both the VSCs give on

$$\frac{V_{x_1o} + V_{x_2o}}{2} = V_{xo} + \frac{R_{CI}}{2}I_x + \frac{(L_s - L_m)}{2}\frac{dI_x}{dt} \tag{5}$$

By neglecting the resistance of the coils and assuming a strong magnetic coupling $L_m \approx L_s$ ($k \cong 1$), the voltage of the common connection point with respect to the reference o is

$$V_{xo} = \frac{1}{2}(V_{x_1o} + V_{x_2o}) \tag{6}$$

which demonstrates three-level voltage waveforms as shown in Fig. 2(b). As a result, the volume of the harmonic filter components can be reduced.

From (5), it is evident that the impact of the CI on the line current is negligible. On the other hand, CI significantly influences the circulating current and the dynamics of the circulating current is represented as

$$\frac{dI_{x,c}}{dt} = \frac{1}{4L_s}(V_{x_1o} - V_{x_2o}) \tag{7}$$

It is clear from (7) that the inductance offered to the circulating current is four times the self-inductance L_s. Therefore effective suppression of the circulating current can be achieved.

By solving the simplified reluctance model, as shown in Fig. 3(b), the resultant flux in the core is given as

$$\phi_x = \frac{2N_{CI}}{2(\Re_l + \Re_y)}I_{x,c} \tag{8}$$

where N_{CI} is the number of turns, $\Re_l$ is the reluctance of the limb, and $\Re_y$ is the reluctance of the yoke. Using (8), the difference of the pole voltages are obtained as

$$(V_{x_1o} - V_{x_2o}) = -\frac{4N_{CI}^2}{\Re}\frac{dI_{x,c}}{dt} \tag{9}$$

using (7) and (9), the self-inductance $L_s = -N^2/\Re$ and the inductance offered to the circulating current is given as

$$L_c = 4N_{CI}^2 \mu_0 \mu_r A_{c,CI}/l_m \tag{10}$$

where μ_0 is the permeability of free space, μ_r is the relative permeability, l_m is the mean magnetic length, and $A_{c,CI}$ is the core cross-section area. Using (8) and (9), the resultant flux can be given as

$$\phi_x = \frac{1}{2N_{CI}} \int (V_{x_1o} - V_{x_2o})\, dt \tag{11}$$

and the flux density in the core is

$$B_x = \frac{1}{2N_{CI}A_{c,CI}} \int (V_{x_1o} - V_{x_2o})\, dt \tag{12}$$

As it is evident from (12), the flux density is dependent on the product of the number of turns and the cross-section area ($N_{CI}A_{C,CI}$) and the time integral of the pole voltage difference $\int(V_{x_1o}-V_{x_2o})dt$. The $\int(V_{x_1o}-V_{x_2o})dt$ depends on the PWM scheme used [9], [12] and cycle-by-cycle balancing of the $\int(V_{x_1o}-V_{x_2o})dt$ is required (dc flux linkage is required to be zero over a switching cycle) to ensure saturation free operation of the CI without oversizing it.

B. Modulation of Parallel VSCs

Two approaches are possible for the modulation of the parallel interleaved VSCs:

1) Modulation of the individual VSCs with phase-shifted carrier signals.
2) Considering parallel Two Level (2L) VSCs as a one single converter and modulating them as a multi-level converter.

1) Two-level Modulation Schemes with Phase-Shifted Carriers: The carrier comparison approach with the Phase-Shifted Carrier (PSC) modulator is adopted for the 2L modulation, where the carrier signals of two VSCs are phase-shifted by an interleaving angle of 180°, as shown in Fig. 4(a). This approach is easy to implement and widely reported in the literature [18], [19]. Following PWM schemes are evaluated under PSC modulator:

1) 2L centralized Space Vector Modulation (SVM) [20].
2) 2L 60° Discontinuous PWM (DPWM1) [20].

2) Phase Disposition Modulation: The carrier based Phase Disposition (PD) modulation is considered. However, the conventional approach of using two co-phasal carrier signal can not be readily applied as it introduces dc voltage in the pole voltage difference $(V_{x_1o} - V_{x_2o})$ [21]. Therefore PD modulator using the carrier rotation is used, as shown in Fig. 4(b). However dc volt-sec appears during the band transition (transition from positive value of the sampled reference voltage to the negative value and vice-versa), as shown in Fig. 4(b). This may lead to the saturation of the CI. One of the possible solution is to introduce additional switching of the semiconductor devices during the band transition, which leads to an increase in the switching losses. Following PWM schemes are evaluated under the PD modulator:

1) 3L Space Vector Modulation (3L-SVM) [22].
2) 2L 60° Discontinuous PWM with PD modulator.

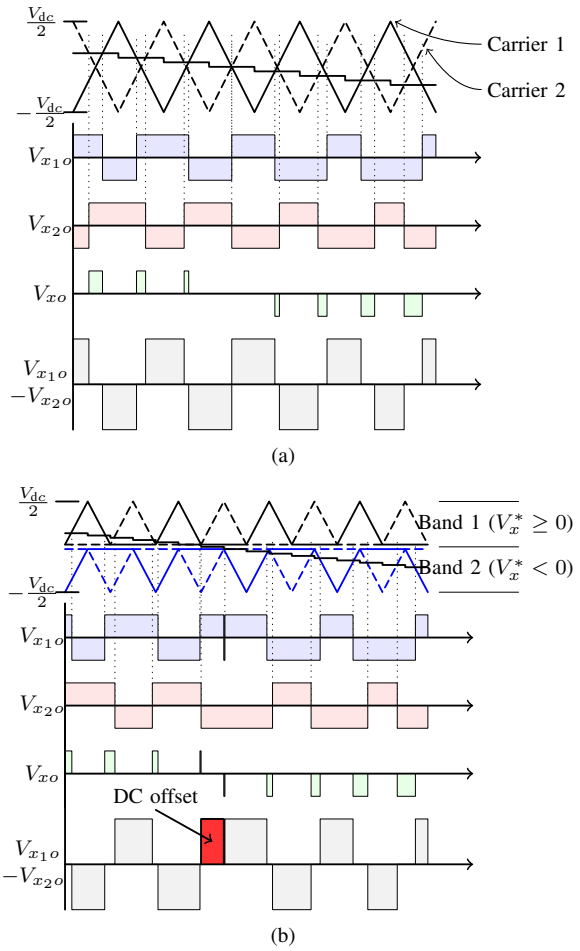

Fig. 4. Modulators based on the carrier comparison for parallel interleaved VSCs. (a) PSC modulator: Phase-shifted carrier signals with interleaving angle of 180° for two-level modulation schemes, (b) PD modulator: The carrier signals are arranged in two carrier bands ($V_x^* \geq 0$ and $V_x^* < 0$) with two phase-shifted carrier signals in each of the bands.

III. Harmonic Performance Assessment and LCL Filter Design

A. Normalized Weighted Total Harmonic Distortion

The harmonic performance of all the considered PWM schemes is compared by evaluating the Normalized Weighted Total Harmonic Distortion (NWTHD), which is defined as

$$\text{NWTHD} = \frac{M}{V_f}\sqrt{\sum_{h=2}^{\infty}(V_h/h)^2} \tag{13}$$

where V_f is the fundamental component and V_h is the magnitude of the hth harmonic component. The NWTHD of all the

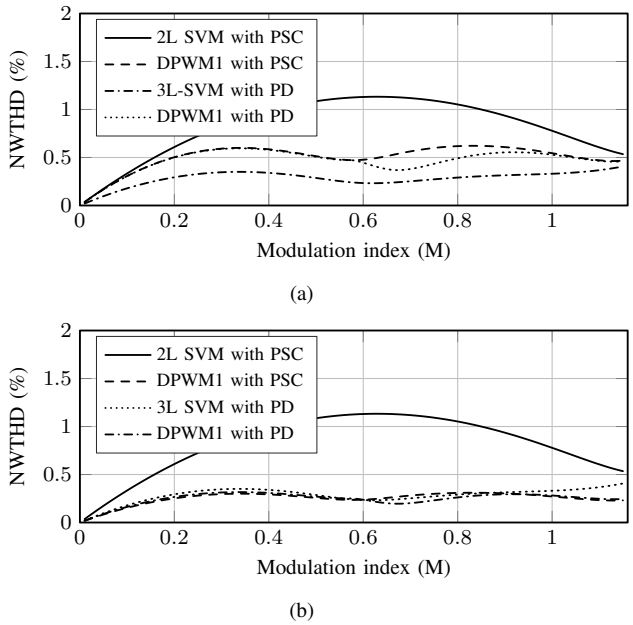

Fig. 5. Theoretical variation of the NWTHD with a modulation index M. (a) The switching frequency is taken to be the same. (b) The switching frequency is varied such that the constant switching losses are achieved.

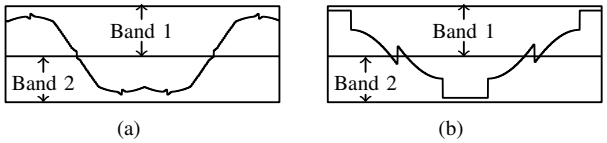

Fig. 6. Modulating signal waveform over a fundamental frequency cycle. (a) Three-level space vector modulation (3L-SVM), (b) Two-level 60° discontinuous PWM (DPWM1).

PWM schemes is shown in Fig. 5(a). The carrier frequency is taken to be the same for all the cases. The 3L-SVM with PD modulator demonstrates superior harmonic performance, whereas 2L SVM with PSC modulator has the worst harmonic performance. Since the carrier frequency is the same for all schemes, the switching losses are different for continuous and discontinuous PWM schemes.

In a fundamental cycle, the DPWM1 scheme clamps the output terminals of the VSCs to the positive and the negative terminals of the dc-link for a 60° interval each and the clamping intervals of 60° are arranged around the positive and negative peak of the fundamental reference voltage. The WECS typically operates with a power factor close to unity. In this case, the switching losses can be reduced up to 50% by using the DPWM1.

Under the PD modulator, two additional commutations are required during each band transition. For the 3L SVM, two such band transitions happen in a fundamental cycle, whereas in DPWM1 scheme, the band transition of the modulating signal happens six times (for $2/3 \leq M \leq 2/\sqrt{3}$), as shown in Fig. 6. Moreover, additional transitions may also be required during the sector transition. Considering this, the carrier frequencies of all the PWM schemes are adjusted to achieve the same switching losses under the unity power factor load condition as given in Table I.

TABLE I
ADJUSTED CARRIER FREQUENCIES TO ACHIEVE CONSTANT SWITCHING LOSSES UNDER UNITY POWER FACTOR LOAD.

PWM Scheme	Carrier frequency F_c
2L-SVM with PSC	1250 Hz
DPWM1 with PSC	2500 Hz
3L-SVM with PD	1200 Hz
DPWM1 with PD	2250 Hz

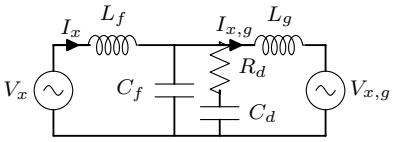

Fig. 7. Single phase equivalent circuit of the LCL filter with parallel R_d/C_d damping branch. V_x and $V_{x,g}$ are the phase voltage and grid voltage of phase x, respectively.

The NWTHD with the adjusted carrier frequency is shown in Fig. 5(b). The DPWM1 with both the PSC and PD modulator outperforms 2L-SVM with PSC modualtor and 3L-SVM with PD modulator. For the modulation index close to unity (which is the case for the grid-connected WECS), the NWTHD of the DPWM1 with PSC modulator is lowest, as shown in Fig. 5(b).

B. Impact on the Harmonic Filter

From the NWTHD, it is difficult to draw a conclusion about the size of the harmonic filter components and the information may not be readily useful for grid-connected converters. The value of the LCL harmonic filter components for a 2 MW, 690 V WECS under different PWM schemes are evaluated. The single-line diagram of the LCL filter is shown in Fig. 7. A parallel R_d/C_d damping branch is employed to damp the resonance introduced by the LCL filter. The WECS is considered to be connected to the medium-voltage network using a step-up transformer and the leakage inductance of this transformer (which is taken to be 0.08 pu) is considered to be the part of the grid-side inductance of the LCL filter.

1) Design of the LCL Filter: The LCL harmonic filter is designed as per the procedure outlined in [23] to meet the harmonic injection limits specified by the German Association of Energy and Water Industries (BDEW). The spectrum comprises the maximum values of the individual voltage harmonic components of the resultant voltage, over the entire operating range is obtained and it is defined as a Virtual Voltage Harmonic Spectrum (VVHS) [23]. The harmonic current injection limit for a generator connected to the medium-voltage network, specified by BDEW [3], [23], [24], is considered in this paper. The permissible harmonic current injection is determined by the apparent power of the WECS and the Short-Circuit Ratio (SCR) at the Point of the Common Coupling (PCC). The maximum current injection limit of the individual harmonic components up to 9 kHz is specified in the standard. Using the specified values of the permissible harmonic injection and VVHS, the required

TABLE II
LCL HARMONIC FILTER COMPONENTS FOR DIFFERENT MODULATION SCHEMES WITH ADJUSTED CARRIER FREQUENCY TO ACHIEVE THE SAME SWITCHING LOSSES.

PWM Scheme	L_f	L_g (incl. transformer leakage 0.08 pu)	C_f	C_d
2L-SVM with PSC	151.5 μH (0.22 pu)	82.6 μH (0.12 pu)	2200 μF (0.15 pu)	1100 μF (0.075 pu)
DPWM1 with PSC	68.8 μH (0.1 pu)	55.1 μH (0.08 pu)	1200 μF (0.08 pu)	600 μF (0.04 pu)
3L-SVM with PD	110 μH (0.16 pu)	55.1 μH (0.08 pu)	1900 μF (0.13 pu)	950 μF (0.065 pu)
DPWM1 with PD	61.9 μH (0.09 pu)	55.1 μH (0.08 pu)	880 μF (0.06 pu)	440 μF (0.03 pu)

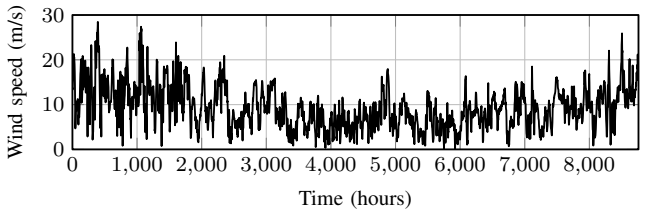

Fig. 8. Recorded wind data over a year with three hourly sampling rate.

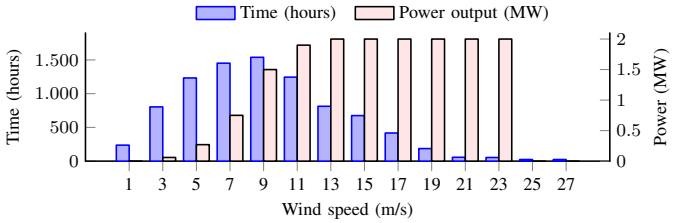

Fig. 9. Assumed wind speed distribution and power produced. The total energy production in a year is 10548 MWh.

admittance for the hth harmonic component is obtained as

$$Y_h^* = \frac{I_{h,BDEW}^*}{V_{h,VVHS}} \tag{14}$$

where $I_{h,BDEW}^*$ is the specified BDEW current injection limit of the hth harmonic component (refer to [3]) and $V_{h,VVHS}$ is the maximum values of the hth harmonic components over the entire operating range. The value of the filter parameters are then chosen such that the designed filter has a lower admittance than the required value of the filter admittance for all the harmonic frequency components of interest (upto 180th harmonic frequency component in the case of the BDEW standard) [5], [6]. The required value of the harmonic filter components under the same switching loss conditions for the considered PWM schemes are given in Table II. The smallest values of the harmonic filter components are obtained using the DPWM1 with the PD modulator.

2) Design of the Converter-Side Inductor: Since the leakage inductance of the step-up transformer is sufficient as a grid-side inductance of the LCL filter, only the size of the converter-side inductor is evaluated. An optimized design of the converter-side inductor is carried out using the design procedure outlined in [25]. Recorder wind speed data at Aalborg University over a one year period with three hourly sampling rate is shown in Fig. 8. Since, the wind speed varies in a large range, the power processed by the WECS also varies in wide range, as shown in Fig. 9. As a result, suboptimal performance will be achieved if the converter-side inductor is optimized at the specific loading condition. Therefore, instead of optimizing the inductor losses at specific loading condition, the energy loss for a given load profile is minimized. In addition to the energy loss minimization, the volume minimization is also considered and multi-objective optimization has been carried out.

The multi-objective optimization has been performed, which minimizes a vector of objectives $F(X)$ and returns the optimal values of the design variables X.

$$\min F(X) \tag{15}$$

where

$$F(X) = [F_1(X), F_2(X)] \tag{16}$$

where $F_1(X)$ returns the energy loss (kWh). The total losses $(P_{fe} + P_{cu})$ are evaluated for each of the loading conditions shown in Fig. 9 and the total energy losses (kWh) are obtained as

$$F_1(X) = \frac{1}{1000} \sum_{i=1}^{j} (P_{fe_i} + P_{cu_i}) T_i \tag{17}$$

where T_i is the number of hours during which the WECS output power is P_i and associated losses are $(P_{fe_i} + P_{cu_i})$.

$F_2(X)$ returns the volume of the active parts of the inductor (ltr.) and it is given as

$$F_2(X) = (V_{fe} + V_{cu}) * 1000 \tag{18}$$

where V_{fe} is the volume of the magnetic material and V_{cu} is the total volume of all the coils. The parameters that are optimized are

$$X = [N_{L_f}\ B_m\ J\ m\ W_c]^T \tag{19}$$

where N_{L_f} is the number of turns, B_m is the maximum flux density, J is the current density, m is the number of layers in the windings, and W_c is the width of the coil.

The Improved Generalized Steinmetz Equation (IGSE) [26], [27] is used to calculate the core losses. The core losses per unit volume is given as

$$P_{fe,v} = \frac{1}{T} \int_0^T k_i \left| \frac{dB(t)}{dt} \right|^{\alpha} (\Delta B)^{\beta - \alpha} dt \tag{20}$$

where α, β and k_i are the constants determined by the material characteristics. ΔB is the peak-to-peak value of the flux density and T is the switching interval. The flux waveform

TABLE III

PARAMETER VALUES OF THE CONVERTER-SIDE INDUCTOR OF THE LCL FILTER. A_{c,L_f} AND A_{cu,L_f} ARE THE CROSS-SECTION AREA OF THE CORE AND COIL, RESPECTIVELY. P_{cu} IS THE COPPER LOSS AND P_{fe} IS THE CORE LOSS.

PWM Scheme	L_f	N_{L_f}	B_m	A_{c,L_f}	A_{cu,L_f}	Volume	Energy loss	Losses at full-load (2 MW)		
	μH		T	cm^2	mm^2	Ltr.	kWh	P_{cu}(kW)	P_{fe}(kW)	Total (kW)
2L-SVM with PSC	151.5	27	1.55	98	594	56.8	63570	5.51	4.66	10.18
DPWM1 with PSC	68.8	24	1.55	52	586	31.1	80904	4.17	7.36	11.54
3L-SVM with PD	110	26	1.54	75	596	45	77725	4.69	6.77	11.47
DPWM1 with PD	61.9	28	1.52	43	592	32	94764	4.63	8.75	13.39

has major and minor loops and these loops are evaluated separately, as outlined in [25].

The copper loss is evaluated by considering the ac resistance of the winding, which takes into account the skin and proximity effects [28]. The total winding losses of all three coils are [29]

$$P_{cu} = 3R_{dc}\sum_{h=1}^{\infty} k_{p_h} I_{x_h}^2 \tag{21}$$

where

$$k_{p_h} = \sqrt{h}\Delta\Big[\frac{\sinh(2\sqrt{h}\Delta)+\sin(2\sqrt{h}\Delta)}{\cosh(2\sqrt{h}\Delta)-\cos(2\sqrt{h}\Delta)} + \frac{2}{3}(m^2-1)\frac{\sinh(\sqrt{h}\Delta)-\sin(\sqrt{h}\Delta)}{\cosh(\sqrt{h}\Delta)+\cos(\sqrt{h}\Delta)}\Big] \tag{22}$$

and $\Delta = T_c/\delta$ and R_{dc} and R_{ac} are the dc and the ac resistance of the coil, respectively. m is the number of layers in the coil, T_c is the thickness of the conductor, and δ is the skin depth. I_{x_h} is the hth harmonic frequency component of the line current I_x.

The non-inferior (Pareto optimal) solutions are obtained using the multi-objective optimization as shown in Fig. 10. Out of these several possible design solutions, one suitable solution has been selected for each of the PWM schemes and the parameter values of the selected design are given in Table III. The energy loss is lowest when 2L-SVM with PSC is used. However, the volume is maximum in that case. The volume of the converter-side inductor is almost the same in the case of the DPWM1 with PSC and DPWM1 with PD. However, it is important to note that the shunt capacitance requirement for the DPWM1 with PD modulator is 26.6% smaller than that of the DPWM1 with PSC. The loss density (which is the ratio of the losses at full load to the available surface area for the heat dissipation) determines the cooling capacity requirement, which is highest in the case of the DPWM1 with PD.

IV. IMPACT ON THE COUPLED INDUCTOR

The physical arrangement of the CI is shown in Fig. 3. The flux density for the CI is given by (12) and the maximum value of the flux density is obtained as

$$B_{x_{max}} = \frac{V_{\rm dc}}{8N_{CI}A_{c,CI}F_c} \tag{23}$$

where $V_{\rm dc}$ is the dc-link voltage and F_c is the carrier frequency. Using this, the product of the number of turns N and the cross-sectional area A_c is given as

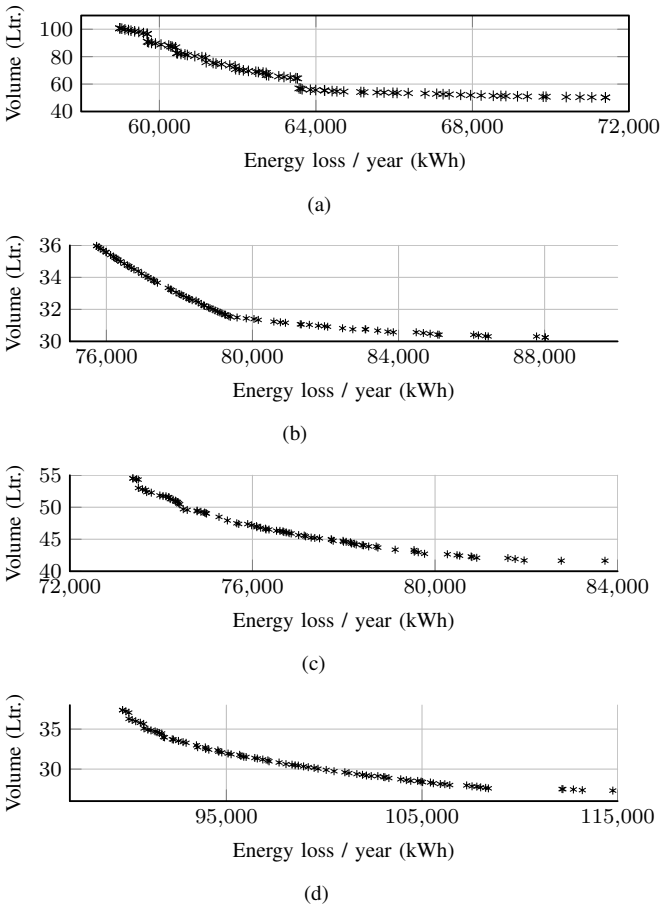

Fig. 10. Calculated volume and energy loss of the converter-side inductor for different Pareto optimal solutions for a load profile with the annul energy production of 10548 MWh. (a) 2L-SVM with PSC, (b) DPWM1 with PSC, (c) 3L-SVM with PD, (d) DPWM1 with PD.

$$N_{CI}A_{c,CI} = V_{\rm dc}/(8B_{x_{max}}F_c) \tag{24}$$

For the given dc-link voltage and the magnetic material (therefore $B_{x_{max}}$), the product of the number of turns N_{CI} and the cross-sectional area $A_{c,CI}$ is inversely proportional to the carrier frequency. As a result, higher switching frequency operation leads to a smaller size of the CI. Under the same switching losses condition, the carrier frequency in the case of the DPWM1 is higher than the continuous PWM schemes. As a result, smaller size of the CI is expected with the DPWM1.

The multi-objective optimization of the CI has been also carried out. Considering equal current sharing between the

TABLE IV
PARAMETER VALUES OF THE COUPLED INDUCTOR. AIR GAP OF 1 mm IS CONSIDERED IN ALL CASES.

PWM Scheme	L_c mH	N_{CI}	B_m T	$A_{c,CI}$ cm^2	$A_{cu,CI}$ mm^2	Volume Ltr.	Energy loss kWh	Losses at full-load (2 MW) P_{cu}(W)	P_{fe}(W)	Total (W)
2L-SVM with PSC	7.3	17	1.11	59	304	12.2	3933	443	228	671
DPWM1 with PSC	7.8	18	0.82	37	301	8.7	4048	385	273	658
3L-SVM with PD	8.4	20	1.14	49	297	12.1	4234	468	253	721
DPWM1 with PD	6.7	20	0.94	32	298	8.4	4743	431	328	759

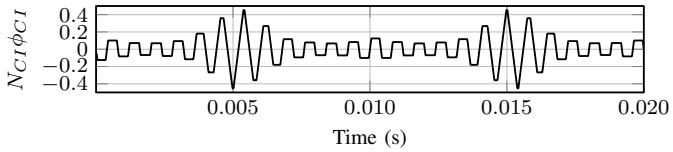

Fig. 11. CI flux linkage over a complete fundamental period. The flux linkage is normalized to $V_{\text{dc}}T_s$.

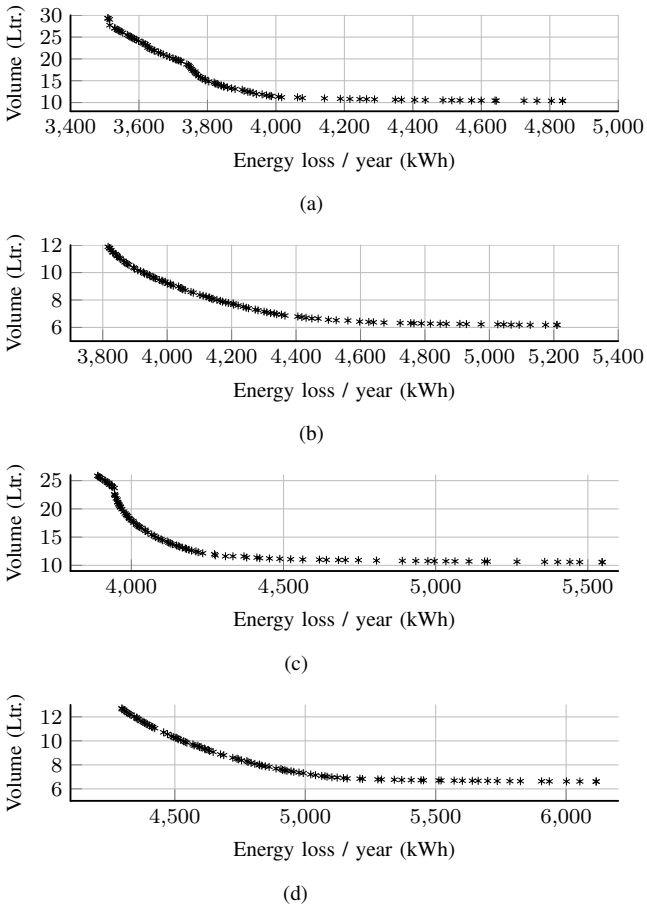

Fig. 12. Calculated volume and energy loss of the coupled inductor for different Pareto optimal solutions for a load profile with the annul energy production of 10548 MWh. (a) 2L-SVM with PSC, (b) DPWM1 with PSC, (c) 3L-SVM with PD, (d) DPWM1 with PD.

parallel VSCs, the fundamental component of the flux in the CI is absent. As a result, the CI only experiences switching frequency flux excitation, as shown in Fig. 11. In this case, the core losses can be accurately evaluated using the IGSE [26]. The copper losses are also evaluated by considering the skin and proximity effects. The VSC leg current flows through

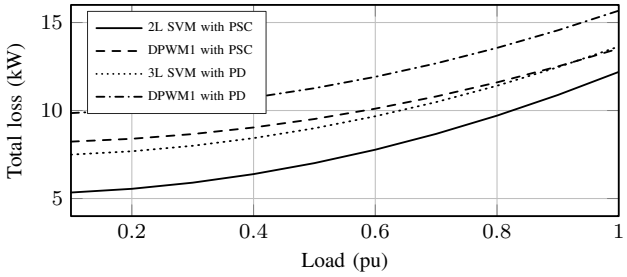

Fig. 13. Variation of the total losses of the inductive components (converter-side inductor of the LCL filter and three coupled inductors) with the load.

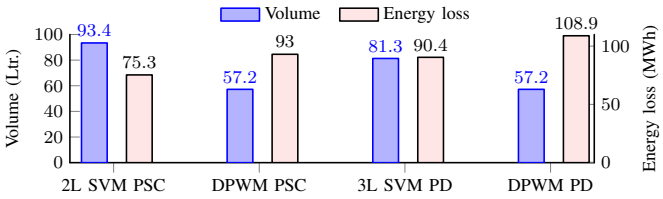

Fig. 14. Volume and the energy losses of all the inductive components (converter-side inductor of the LCL filter and three coupled inductors).

the coils of the CI and it can be decomposed into circulating current component and the resultant line current components. Effects of both of these current components are considered in the copper loss evaluation of the CI.

The Pareto optimal solutions for all the considered PWM schemes are shown in Fig. 12. Out of these several possible design solutions, one suitable design is chosen for each case and the parameters of the selected design are given in Table IV. As expected, the use of the DPWM1 leads to lower volume of the CI under the constant switching losses condition. Out of the selected designs, the DPWM1 with PD modulator lead to the highest energy losses.

For the chosen designs, the variation of the total losses of all the inductive components, which include the converter-side inductor of the LCL filter and three CIs, with the load is shown in Fig. 13. The losses in the case of the 2L SVM with PSC modulator is lowest and the volume of the inductive components is highest, as shown in Fig. 14. The volume of the inductive components in DPWM1 scheme with both the PSC and PD modulator is the same. However, the energy losses in the DPWM1 with the PSC modulator is lower than the DPWM1 with the PD modulator. In conclusion, the use of the DPWM scheme with the PSC modulator gives best compromise between the energy loss and the volume of the inductive components for the grid-connected parallel interleaved VSCs.

V. Conclusion

The volume and the losses of the converter-side inductor of the LCL harmonic filter and the CI for the grid-connected WECS with two parallel interleaved VSCs under different PWM schemes are evaluated in this paper. The comparative evaluation has been carried out with the adjusted carrier frequencies to achieve the switching losses to be the same in all the PWM schemes for unity power factor load. A multi-objective optimization to minimize the energy loss and volume is carried out for all considered modulation schemes. Pareto optimal solutions are obtained and out of several possible solutions, one suitable solution for each PWM schemes is chosen. The DPWM1 scheme with both the PSC and PD modulator leads to the lowest volume of the inductive components. However, the energy losses are higher compared to the continuous PWM schemes. The energy losses in the case of the DPWM1 with PSC modulator is 14.6% smaller than that of the DPWM1 with PD modulator. For the wind profile considered in this paper, the energy production of 2 MW WECS is 10548 MWh. When DPWM1 with the PSC modulator is used with the chosen design, the yearly energy loss in the inductive components is calculated to be 93 MWh (0.88%).

Acknowledgments

The authors would like to thank the Intelligent Efficient Power Electronics (IEPE) and HARMONY project for supporting the related research.

References

[1] F. Blaabjerg, M. Liserre, and K. Ma, "Power electronics converters for wind turbine systems," *IEEE Trans. Ind. Appl.*, vol. 48, no. 2, pp. 708–719, March 2012.

[2] F. Blaabjerg and K. Ma, "Future on power electronics for wind turbine systems," *IEEE J. Emerging Sel. Topics Power Electron.*, vol. 1, no. 3, pp. 139–152, Sept 2013.

[3] "Technical guidline: Generating plants connected to the medium-voltage network." BDEW Bundesverband der Energie- und Wasserwirtschaft e.V., [Online]. Available: http://www.bdew.de, 2008.

[4] M. Liserre, R. Cardenas, M. Molinas, and J. Rodriguez, "Overview of multi-MW wind turbines and wind parks," *IEEE Trans. Ind. Electron.*, vol. 58, no. 4, pp. 1081–1095, April 2011.

[5] G. Gohil, L. Bede, R. Teodorescu, T. Kerekes, and F. Blaabjerg, "Design of the trap filter for the high power converters with parallel interleaved VSCs," in *Proc. 40th Annual Conference on IEEE Industrial Electronics Society, IECON 2014*, Oct 2014, pp. 2030–2036.

[6] G. Gohil, L. Bede, R. Teodorescu, T. Kerekes, and F. Blaabjerg, "Line filter design of parallel interleaved vscs for high-power wind energy conversion systems," *IEEE Trans. Power Electron.*, vol. 30, no. 12, pp. 6775–6790, Dec 2015.

[7] Z. Xu, R. Li, H. Zhu, D. Xu, and C. Zhang, "Control of parallel multiple converters for direct-drive permanent-magnet wind power generation systems," *IEEE Trans. Power Electron.*, vol. 27, no. 3, pp. 1259–1270, March 2012.

[8] R. Maheshwari, G. Gohil, L. Bede, and S. Munk-Nielsen, "Effect of dead-time in interleaved pwm for two parallel-connected inverters," in *17th European Conference on Power Electronics and Applications*, Sept 2015, pp. 1–7.

[9] G. Gohil, R. Maheshwari, L. Bede, T. Kerekes, R. Teodorescu, M. Liserre, and F. Blaabjerg, "Modified discontinuous pwm for size reduction of the circulating current filter in parallel interleaved converters," *IEEE Trans. Power Electron.*, vol. 30, no. 7, pp. 3457–3470, July 2015.

[10] R. Maheshwari, G. Gohil, L. Bede, and S. Munk-Nielsen, "Analysis and modelling of circulating current in two parallel-connected inverters," *IET Power Electronics*, vol. 8, no. 7, pp. 1273–1283, 2015.

[11] F. Ueda, K. Matsui, M. Asao, and K. Tsuboi, "Parallel-connections of pulsewidth modulated inverters using current sharing reactors," *IEEE Trans. Power Electron.*, vol. 10, no. 6, pp. 673–679, Nov 1995.

[12] G. Gohil, L. Bede, R. Maheshwari, R. Teodorescu, T. Kerekes, and F. Blaabjerg, "Parallel interleaved VSCs: influence of the PWM scheme on the design of the coupled inductor," in *Proc. 40th Annual Conference on IEEE Industrial Electronics Society, IECON 2014*, Oct 2014, pp. 1693–1699.

[13] G. Gohil, L. Bede, R. Teodorescu, T. Kerekes, and F. Blaabjerg, "An integrated inductor for parallel interleaved three-phase voltage source converters," *IEEE Trans. Power Electron.*, vol. 31, no. 5, pp. 3400–3414, May 2016.

[14] G. Gohil, L. Bede, R. Teodorescu, T. Kerekes, and F. Blaabjerg, "An integrated inductor for parallel interleaved vscs and pwm schemes for flux minimization," *IEEE Trans. Ind. Electron.*, vol. 62, no. 12, pp. 7534–7546, Dec 2015.

[15] G. Gohil, L. Bede, R. Teodorescu, T. Kerekes, and F. Blaabjerg, "Magnetic integration for parallel interleaved vscs connected in a whiffletree configuration," *IEEE Trans. Power Electron.*, [Online early access], DOI: 10.1109/TPEL.2015.2514182, 2016.

[16] G. Gohil, L. Bede, R. Teodorescu, T. Kerekes, and F. Blaabjerg, "Dual converter fed open-end transformer topology with parallel converters and integrated magnetics," *IEEE Trans. Ind. Electron.*, [Online early access], DOI: 10.1109/TIE.2016.2548999.

[17] G. Gohil, "Modulation and circulating current suppression for parallel interleaved voltage source converters," Ph.D. dissertation, Aalborg University, Denmark, March 2016.

[18] K. Xing, F. Lee, D. Borojevic, Z. Ye, and S. Mazumder, "Interleaved PWM with discontinuous space-vector modulation," *IEEE Trans. Power Electron.*, vol. 14, no. 5, pp. 906–917, 1999.

[19] S. Miller, T. Beechner, and J. Sun, "A comprehensive study of harmonic cancellation effects in interleaved three-phase VSCs," in *Proc. IEEE Power Electronics Specialists Conference, 2007. PESC 2007.*, 2007, pp. 29–35.

[20] D. G. Holmes and T. A. Lipo, *Pulse Width Modulation for Power Converters: Principles and Practice*. Hoboken, NJ: Wiley-IEEE Press, 2003.

[21] B. Cougo, G. Gateau, T. Meynard, M. Bobrowska-Rafal, and M. Cousineau, "PD modulation scheme for three-phase parallel multilevel inverters," *IEEE Trans. Ind. Electron.*, vol. 59, no. 2, pp. 690–700, 2012.

[22] B. P. McGrath, D. G. Holmes, and T. Lipo, "Optimized space vector switching sequences for multilevel inverters," *IEEE Trans. Power Electron.*, vol. 18, no. 6, pp. 1293–1301, Nov 2003.

[23] A. Rockhill, M. Liserre, R. Teodorescu, and P. Rodriguez, "Grid-filter design for a multimegawatt medium-voltage voltage-source inverter," *IEEE Trans. Ind. Electron.*, vol. 58, no. 4, pp. 1205–1217, 2011.

[24] S. Araujo, A. Engler, B. Sahan, and F. Antunes, "LCL filter design for grid-connected NPC inverters in offshore wind turbines," in *Proc. Power Electronics, 2007. ICPE '07. 7th Internatonal Conference on*, 2007, pp. 1133–1138.

[25] G. Gohil, L. Bede, R. Teodorescu, T. Kerekes, and F. Blaabjerg, "Optimized integrated harmonic filter inductor for dual-converter fed open-end transformer topology," *IEEE Trans. Power Electron.*, [Online early access], DOI: 10.1109/TPEL.2016.2562679.

[26] K. Venkatachalam, C. Sullivan, T. Abdallah, and H. Tacca, "Accurate prediction of ferrite core loss with nonsinusoidal waveforms using only steinmetz parameters," in *Computers in Power Electronics, 2002. Proceedings. 2002 IEEE Workshop on*, 2002, pp. 36–41.

[27] J. Li, T. Abdallah, and C. Sullivan, "Improved calculation of core loss with nonsinusoidal waveforms," in *Industry Applications Conference, 2001. Thirty-Sixth IAS Annual Meeting. Conference Record of the 2001 IEEE*, vol. 4, 2001, pp. 2203–2210 vol.4.

[28] P. Dowell, "Effects of eddy currents in transformer windings," *Proceedings of the Institution of Electrical Engineers,*, vol. 113, no. 8, pp. 1387–1394, August 1966.

[29] W. Hurley, E. Gath, and J. Breslin, "Optimizing the ac resistance of multilayer transformer windings with arbitrary current waveforms," *IEEE Trans. Power Electron.*, vol. 15, no. 2, pp. 369–376, Mar 2000.